frontiers | Frontiers in Marine Science

TYPE Original Research
PUBLISHED 02 December 2025
DOI 10.3389/fmars.2025.1707329

OPEN ACCESS

EDITED BY
Eun Young Lee,
University of Vienna, Austria

REVIEWED BY
Yang Xiang,
University of Washington, United States
Shengxiong Yang,
Guangzhou Marine Geological Survey, China

*CORRESPONDENCE
Donghoon Seoung
dseoung@jnu.ac.kr
Yongmoon Lee
lym1229@pusan.ac.kr

†These authors have contributed equally to this work

RECEIVED 17 September 2025
REVISED 11 November 2025
ACCEPTED 18 November 2025
PUBLISHED 02 December 2025

CITATION
Kwon S, Jung E, Kong J, Seoung D, Yang K, Jung J, Ko Y and Lee Y (2025) Deep-sea environmental conditions reflected in mineral phases of manganese nodules and their implications for Ni, Co, and Cu geochemistry. *Front. Mar. Sci.* 12:1707329. doi: 10.3389/fmars.2025.1707329

Deep-sea environmental conditions reflected in mineral phases of manganese nodules and their implications for Ni, Co, and Cu geochemistry

Sunki Kwon[1†], Eunji Jung[2†], Jeongmin Kong[3], Donghoon Seoung[4*], Kiho Yang[1,5], Jaewoo Jung[6], Youngtak Ko[6] and Yongmoon Lee[1,3*]

[1]Institute for Future Earth, Pusan National University, Busan, Republic of Korea, [2]School of Environment and Energy Engineering, Gwangju Institute of Science and Technology (GIST), Gwangju, Republic of Korea, [3]Department of Geological Sciences, Pusan National University, Busan, Republic of Korea, [4]Department of Earth and Environmental Sciences, Chonnam National University, Gwangju, Republic of Korea, [5]Department of Oceanography, College of Natural Sciences, Pusan National University, Busan, Republic of Korea, [6]Ocean Georesources Research Department, Korea Institute of Ocean Science & Technology, Busan, Republic of Korea

Manganese (Mn) nodules are deep-sea mineral resources that contain critical elements for modern industries, such as nickel (Ni), cobalt (Co), and copper (Cu). As a result, extensive global research has been conducted on the exploration and formation mechanisms of Mn nodules. However, studies investigating the correlation between manganate minerals and critical elements, as well as the deep-sea environment represented by these mineral phases, have been limited. Here, we show the significance of phase transformations in manganate minerals within Mn nodules, in relation to deep-sea formation environments and the geochemical behavior of Ni, Co, and Cu, using basic statistical analysis, machine learning, and hydrothermal experiments. The statistical analysis and machine learning models revealed that the trace amounts of Ni, Co, and Cu exhibit a positive correlation with vernadite, a dominant manganate mineral in Mn nodules. Additionally, hydrothermal experiments demonstrated that under suboxic conditions at temperatures between 120°C and 150°C, Mn nodules undergo mineral phase transformations, forming various minerals, including todorokite, Mn ferrite, fluorapatite, hematite, and goethite. During these transformations, Ni, Co, and Cu were incorporated into the mineral structures of todorokite, fluorapatite, and Mn ferrite, respectively. Therefore, the mineral phases within Mn nodules serve as key indicators not only for understanding their formation environment but also for tracking changes in the geochemical behavior of Ni, Co, and Cu. Furthermore, our methodological approach demonstrates to many researchers how correlations between materials can be validated and utilized using statistical analysis and machine learning techniques.

KEYWORDS

manganese nodules, mineral phases, deep-sea environment, metal ions, geochemistry, machine learning, critical minerals

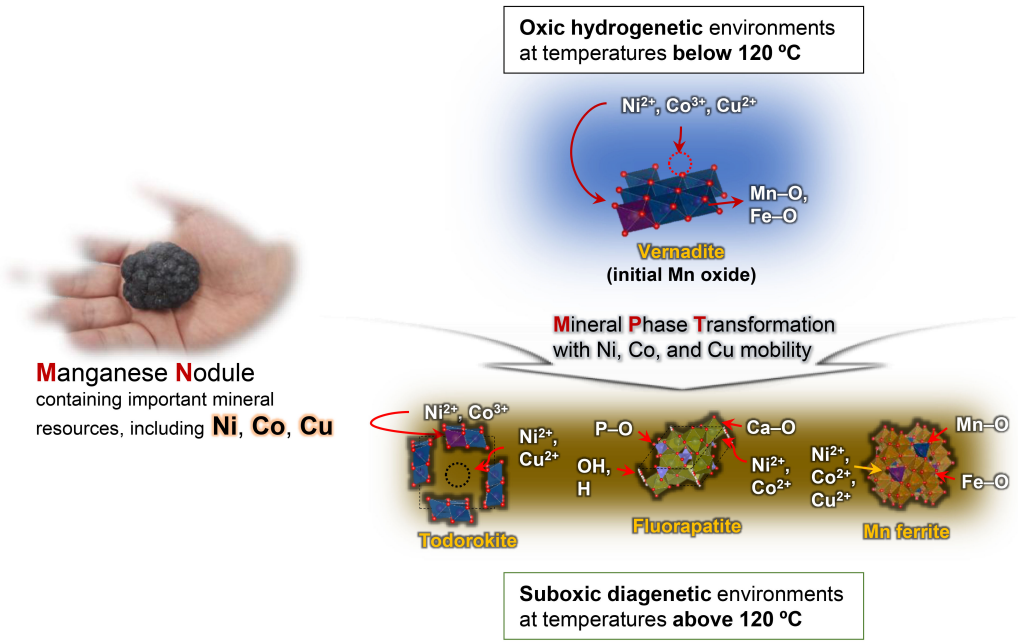

GRAPHICAL ABSTRACT

Introduction

Manganese (Mn) nodules predominantly consist of iron (Fe)-rich Mn oxides and are found in deep-sea environments. These Mn nodules are known to contain significant mineral resources of economic value, including nickel (Ni), cobalt (Co), and copper (Cu) (Jung et al., 2023). They are primarily used in the production of secondary batteries and electronic devices, such as those in electric vehicles (Calvo and Valero, 2022). Recently, the demand for these minerals has increased due to the growth of the eco-friendly renewable energy industry, which aims to mitigate global warming (Calvo and Valero, 2022). As a result, many countries are actively engaging in the exploration and formation mechanisms of deep-sea Mn nodules.

Many previous studies have investigated the physicochemical properties of Mn nodules, such as morphology, structure, mineral phases, and chemical composition, primarily using instruments like X-ray diffraction (XRD), scanning electron microscopy (SEM), inductively coupled plasma mass spectrometry (ICP-MS), and electron probe microanalysis (EPMA) (González et al., 2016; Heller et al., 2018; Wu et al., 2019). In terms of their structural characteristics, Mn oxides in Mn nodules primarily exist as MnO_6 octahedra, which share edges and corners with various structural variants. These oxides exhibit a coexistence of Mn^{3+} and Mn^{4+} (Post, 1999; Wu et al., 2019; Wegorzewski et al., 2020). Representative manganate minerals in Mn nodules, composed of these oxides, include vernadite, birnessite, buserite, and todorokite (Atkins et al., 2014; Vereshchagin et al., 2019; Namgung et al., 2020; Wegorzewski et al., 2020; Jung et al., 2023). Mineralogically, vernadite is a turbostratic phyllomanganate (δ-MnO_2), known as 7 Å and 10 Å vernadite, as well as Fe-vernadite, which dominantly forms in diagenetic and hydrogenetic environments, respectively (Wegorzewski et al., 2020). Birnessite, the primary manganate mineral phase in deep-sea sediments under hydrogenetic environments, consists of layers of MnO_6 octahedra (Atkins et al., 2014). Its interlayer contains a single layer of water molecules, resulting in a basal *d*-spacing of 7 Å, where cations such as Na^+ and K^+ are present. Similarly, buserite, another phyllomanganate mineral, consists of layers of MnO_6 octahedra but differs in that its interlayer contains a double layer of water molecules with Mg^{2+} cations, resulting in a basal *d*-spacing of 10 Å (Atkins et al., 2014; Jung et al., 2023). Todorokite, which forms in diagenetic environments, consists of edge-sharing MnO_6 octahedra and is classified as a tectomanganate mineral with a tunnel structure measuring approximately 10 Å × 10 Å (Atkins et al., 2014; Wegorzewski et al., 2015, 2020). The tunnels of todorokite are generally occupied by hydrated Mg^{2+} cations and other divalent cations (e.g., Ba^{2+}) (Xu et al., 2010). Among these manganate minerals, todorokite has received significant attention due to its role in the geochemical behavior of heavy metals such as Ni, Co, and Cu. Heavy metals adsorbed during the early and late stages of phyllomanganate mineral formation are either incorporated into the mineral structure or exist as outer-sphere complexes within the tunnels during their transformation to todorokite (Heller et al., 2018; Wegorzewski et al., 2020). More precisely, Ni and Cu initially adsorb onto the surfaces of phyllomanganate minerals but gradually become incorporated into the Mn–O octahedra of the mineral structure over time (Peacock, 2009; Peña et al., 2010; Sherman and

Peacock, 2010; Atkins et al., 2014). In contrast, Co primarily exists as hydrated Co^{2+} ions in seawater and as Co^{3+} ions in crusts. When Co^{2+} ions adsorb onto the surface of phyllomanganate minerals, Mn oxides facilitate their oxidation to Co^{3+}, after which they are incorporated into the Mn–O octahedra through isomorphic substitution (Wu et al., 2019; Yang et al., 2024), as the ionic radius of Co^{3+} (0.054 nm) closely matches that of Mn^{4+} (0.053 nm).

Geochemically, Mn nodules formed in hydrogenetic environments (ambient seawater, oxic conditions) exhibit low Mn/Fe ratios (<4) as well as low concentrations of Ni and Cu, but high concentrations of Fe and Co (Kuhn et al., 2017b; Wegorzewski et al., 2020; Jung et al., 2023). The representative manganate minerals in these nodules are turbostratic phyllomanganate minerals (δ-MnO_2), such as vernadite and birnessite, along with an amorphous δ-FeOOH phase (Hein et al., 2013). Conversely, Mn nodules formed in diagenetic environments (porewater in sediments, suboxic conditions) are characterized by high Mn/Fe ratios (>4) and elevated concentrations of Ni and Cu, but lower concentrations of Fe and Co compared to those in hydrogenetic environments (Kuhn et al., 2017b; Wegorzewski et al., 2020; Jung et al., 2023). These diagenetic Mn nodules predominantly contain todorokite, which forms through the mineral phase transformation of phyllomanganate minerals. This suggests that the geochemical behavior of heavy metals is closely linked to manganate mineral phases. Although previous studies have explored the relationship between heavy metals and manganate minerals (Atkins et al., 2014; Wu et al., 2019; Wegorzewski et al., 2020), most have focused exclusively on todorokite. Furthermore, while many studies have examined the formation environments and chemical composition distributions of Mn nodules in deep-sea sediments (Manceau et al., 2014; Wegorzewski et al., 2015; Kuhn et al., 2017b; Vereshchagin et al., 2019; Zawadzki et al., 2022; Huang et al., 2023; Yang et al., 2024), research specifically addressing mineral phase transitions, the associated geochemical behavior of heavy metals, and the inference of deep-sea environmental conditions remains insufficient, particularly in experimental studies using actual Mn nodules.

Our previous study (Jung et al., 2023) also investigated the physicochemical properties of Mn nodules from both the eastern and western Pacific Oceans to classify their formation environments—such as hydrogenetic and diagenetic—and to identify the distribution of corresponding mineral phases. In particular, stacked synchrotron X-ray diffraction data were utilized to precisely characterize the mineral phases within the Mn nodules. The acquired data were then used to determine their specific mineral compositions and quantitative abundances. However, we were unable to explain the geochemical behavior of heavy metals in relation to mineral phases within Mn nodules under deep-sea environmental conditions, mainly due to the limited number of samples, which prevented us from obtaining sufficient data.

Consequently, the specific deep-sea environmental conditions under which certain manganate minerals form, as well as the geochemical behavior of associated heavy metals, remain poorly understood. We hypothesized that heavy metals, such as Ni, Co, and Cu, would exhibit changes in their geochemical behavior during mineral phase transformations from initial manganate minerals to other phases, depending on variations in deep-sea environmental conditions. Therefore, this study aims to investigate the correlations between manganate mineral phases and their chemical compositions, particularly the distribution of heavy metals and the environmental conditions associated with mineral formation, using additional Mn nodules collected from the deep sea. Methodologically, to examine the correlations between various elements, including heavy metals, and manganate minerals, we employed basic statistical analysis methods. Conventional 2D (X–Y) and ternary plot diagrams are useful for intuitive data visualization and for identifying simple relationships. However, these diagrams cannot account for additional variables and are difficult to use for quantification or prediction using mathematical models. In contrast, statistical analysis enables the identification of complex and quantitative relationships between multiple chemical compositions and mineral phases within Mn nodules, based on statistical significance (e.g., the reliability of the results). Additionally, the correlations between heavy metals and mineral phases are cross-validated using machine learning algorithms. While statistical analysis clarifies the significance and correlations among individual variables (e.g., chemical compositions and mineral phases), machine learning can capture more complex, nonlinear relationships by learning from the variables identified as significant in the statistical analysis. This allows for the discovery of hidden patterns and interactions among multiple variables that may not be evident through conventional statistical methods and facilitates the construction of predictive models. In other words, the successful construction of a predictive model implies that strong correlations exist among the variables. Therefore, we employ machine learning as a complementary tool to validate the correlations between heavy metals and mineral phases within Mn nodules. Finally, we will clarify the geochemical behavior of heavy metals associated with manganate mineral phases through experiments designed to simulate deep-sea environmental conditions.

Materials and methods

Materials

The Magellan Seamounts, the study area, are located to the east of the Mariana Trench in the western Pacific Ocean (Figure 1). These seamounts form a discontinuous chain of guyots that were created by large-scale submarine volcanic activity during the Cretaceous period (approximately 120–80 Ma) (Staudigel et al., 1991; Koppers et al., 1998; Yang et al., 2024). They are mainly composed of tholeiitic or alkaline basaltic rocks, and are capped by sediments consisting primarily of volcaniclastics and carbonate rocks. The oxygen minimum zone (OMZ), where dissolved Mn and associated metals are released, occurs at depths of approximately 800–900 m (Glasby et al., 2007). In addition, episodes of phosphogenesis reportedly occurred around 34 Ma, 24 Ma, and 15 Ma, during which foraminiferal and nanofossil sediments were replaced by carbonate fluorapatite (CFA) (Hein et al., 2000; Glasby et al., 2007; Li et al., 2023).

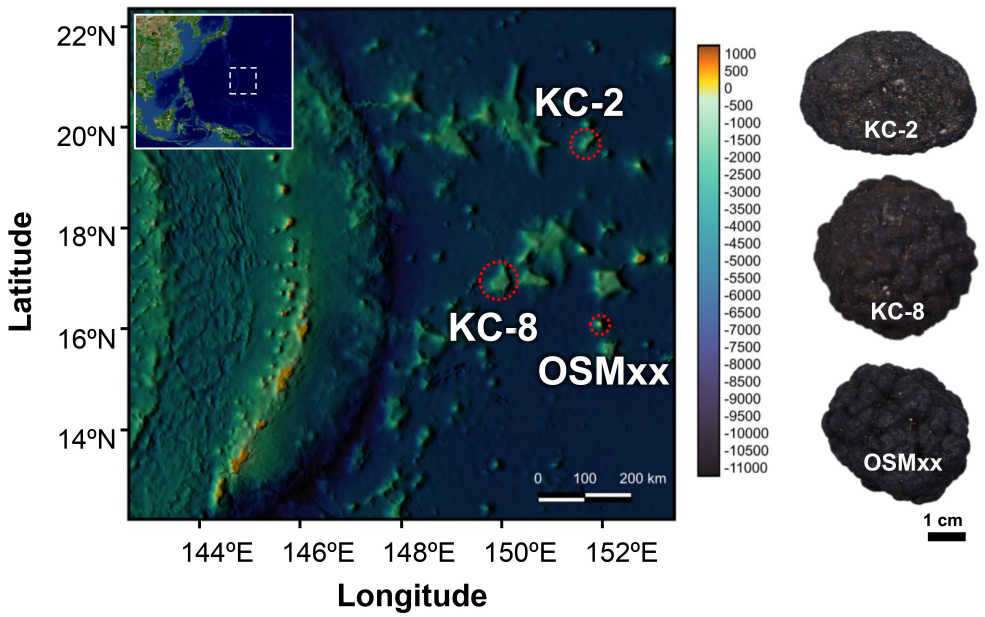

FIGURE 1
Sampling locations of ferromanganese nodules (KC-2, KC-8, and OSMxx) from the Magellan Seamount in the Western Pacific Ocean.

Mn nodules used in this study were collected from Korean Cluster-2 (KC-2, n = 14, depth: 1219 m), Korean Cluster-8 (KC-8, n = 17, depth: 1235 m), and Open Seamount (OSMxx, n = 13, depth: 1597 m), which are part of the Magellan Seamounts, using an epibenthic sledge (Figure 1). The sampling was conducted during the 2021 R/V Isabu Expedition by the Korea Institute of Ocean Science and Technology (KIOST). The Mn nodule samples were first cut in half using a handheld mini saw, and the cross-sections were examined. Upon examining the cross-section of the collected Mn nodules, the core or rim can reveal the presence of marine sediments (Supplementary Figure S1). For this study, the darker regions—primarily composed of manganate minerals—were selected, as the research aimed to investigate the correlation between chemical composition, including heavy metals, and manganate mineral phases, as well as to interpret deep-sea environmental conditions through these phases. Even within the dark regions of the nodules, subtle color differences (e.g., dark brown and black) were observed discontinuously. These areas were sampled using a micro-drill and used as the research material. Of course, the growth structure (from core to rim) of Mn nodules is important for understanding their growth history and the environmental conditions during formation. However, since our focus was on the distribution patterns of heavy metals associated with manganate mineral phases as indicators of deep-sea environmental changes, selective sampling was conducted in visually distinguishable areas. Additionally, Mn nodules typically grow around nuclei such as sediments or fish bone fragments (Wegorzewski et al., 2020). However, unless these materials are significantly aggregated and visible to the naked eye, it is difficult to detect them due to their fine size. As mentioned above, the study area has undergone multiple episodes of phosphatization, so phosphate minerals may occur within the Mn nodules even if they are not derived from sedimentary or fish bone fragment nuclei. Therefore, we recognized that even when selectively sampling the dark, manganate-rich portions, minerals such as quartz, feldspar, or phosphate—originating from sedimentary sources or phosphatization—may still be present. As a result, a total of 403 manganate samples (84 from KC-2, 187 from KC-8, and 132 from OSMxx) were obtained and subsequently pulverized using an agate mortar.

Mineral identification and chemical compositions

The mineral phase and structure of all samples were confirmed by XRD (MiniFlex 600, Rigaku) using CuKα radiation at 40 kV and 15 mA, with a scan speed of 0.5°/min, and a 2θ step size of 0.01°. Mineral qualitative and quantitative analyses, including peak information—full width at half maximum (FWHM) and area—were conducted using SmartLab Studio II software (Rigaku). All samples were analyzed twice after drying at 90°C for 12 h to distinguish between todorokite and buserite (Jung et al., 2023). At this temperature, 10 Å phyllomanganate minerals such as buserite lose interlayer water, causing the interlayer d-spacing to collapse from 10 Å to ~7 Å, whereas the 10 Å peak of todorokite remains unchanged (Wegorzewski et al., 2020; Jung et al., 2023). To distinguish todorokite, it is necessary to additionally consider manganate minerals referred to as thermally stable buserite II (Uspenskaya et al., 1987), which also exhibit a 10 Å (9.6–9.7 Å) Bragg reflection even after heating. However, todorokite shows a peak of ≥ 9.7 Å after heating (Bish and Post, 1989) and a

characteristic high-angle Bragg reflection at approximately 2.40 Å (compared to 2.45 Å for vernadite) (Wegorzewski et al., 2015). In this study, however, the quantitative estimation of todorokite was based on the ~10 Å reflection rather than the 2.40 Å peak. The morphology and chemical composition were determined in triplicate using scanning electron microscopy (SEM, SUPRA25, ZEISS) with energy-dispersive spectroscopy (EDS), calibrated by standard materials from Micro-Analysis Consultants Ltd (MAC), at an accelerating voltage ranging from 10 to 20 kV. For bulk chemical composition analysis, an accelerating voltage of 20 kV was used. When analyzing fine particles, the accelerating voltage was reduced to 10–15 kV to minimize potential compositional interference from adjacent particles resulting from EDS beam penetration. The average values were obtained and utilized.

Statistical analyses and machine learning algorithm

Prior to the statistical analyses, outliers were detected and removed from the data using the Moving Median method with a threshold factor of 3. Based on the chemical compositions and manganate mineral contents, the ANOVA method was used to evaluate whether there was a statistically significant difference between two or more independent groups (Xiao et al., 2012; Jung et al., 2024). Tukey's honestly significant difference (HSD) test was performed to identify specific group differences, with a p-value of ≤ 0.05 considered statistically significant. Linear correlations between the variables were assessed using Pearson's correlation analysis, and hierarchical clustering was applied to examine data similarity. The p-value of ≤ 0.05 was also used as the significance threshold. All statistical analyses were conducted using the XLSTAT add-in software.

Random Forest is a machine learning algorithm that enhances predictive performance by combining multiple decision trees. As an ensemble learning method, it offers high predictive accuracy and the advantage of handling diverse data in parallel (Breiman, 2001; Cutler et al., 2007). For this reason, Random Forest has also been used to develop predictive models for exploration and development in Mn nodule-related studies (Gazis et al., 2018; Gazis and Greinert, 2021; Josso et al., 2023). However, this study applied Random Forest to examine the correlation between manganate minerals and their chemical compositions alongside statistical analyses, rather than to develop a predictive model. In other words, the high performance of a predictive model using Random Forest indicates a strong correlation among the target factors.

To train the Random Forest model to learn the chemical composition and XRD pattern information—such as mineral contents, full width at half maximum (FWHM), and the area of the main peak for manganate minerals—all 403 datasets of manganate minerals were standardized to account for differences in the units of chemical composition and XRD pattern information. Outliers were replaced using spline interpolation. Random Forest training was conducted using Python-based Spyder software. The Python code for performing Random Forest utilized 'RandomForestRegressor,' with 70% of the data used for training, 15% for validation, and 15% for testing. The predictive performance of the model was evaluated using mean squared error (MSE) and R^2, along with a regression graph.

Hydrothermal experiments on mineral phase transformation

Hydrothermal experiments were conducted to investigate the transformation of manganate minerals and the geochemical behavior of heavy metals under deep-sea environmental conditions (oxic and suboxic) using hydrothermal autoclave reactors. The Ni, Co, and Cu contents in all samples were below 2% (Supplementary Table S1). To more clearly examine their behavior during manganate mineral phase transformation, samples with higher concentrations were selected for the experiments.

Under oxic conditions, 0.2 g of each selected sample was mixed with 20 mL of distilled (DI) water, adjusted to pH 3, 7, and 12, in a Teflon beaker [ratio of the sample (g) to DI water (mL) = 1:100]. The mixture was then heated at 150°C for 72 hours. Afterward, it was naturally cooled to room temperature, followed by centrifugation (3500 rpm, 30 min). Finally, the sample was dried at 50°C and collected.

For the suboxic condition experiments, sample preparation was carried out inside a nitrogen-filled glove box. A 0.2 g sample was placed into a 25 mL Teflon bottle designed for hydrothermal autoclave reactors and mixed with 20 mL DI water adjusted to pH 3, 7, and 12. The Teflon bottle containing the mixture was then placed into the hydrothermal autoclave reactor, and the main body and lid were tightly sealed to prevent leakage. Afterward, a furnace heated the reactor at 150°C for 72 hours. Following natural cooling to room temperature, the sample was recovered using centrifugation (3500 rpm, 30 min), then dried at 50°C and collected. Finally, the experiments on manganate mineral phase transformation under specific pH conditions (e.g., seawater) with varying temperatures were conducted using the same sample preparation and procedure as in the suboxic conditions. The pH of DI water was adjusted using hydrochloric acid (HCl, 37%, Sigma-Aldrich) and sodium hydroxide (NaOH, 98%, Sigma-Aldrich). The workflow of this study, including the methodology, is presented in Figure 2.

Results and analysis

Mineralogy, morphology, and chemistry of Mn nodules

Representative XRD patterns of samples from different seamount locations among the 403 analyzed samples are shown in Figure 3. In the case of todorokite, the ~10 Å peak was weak and vernadite was dominant, making it difficult to observe the characteristic 2.40 Å peak of todorokite. However, the Bragg peaks observed after heat treatment are mostly confirmed to be 9.9–10 Å (Figure 3). SEM

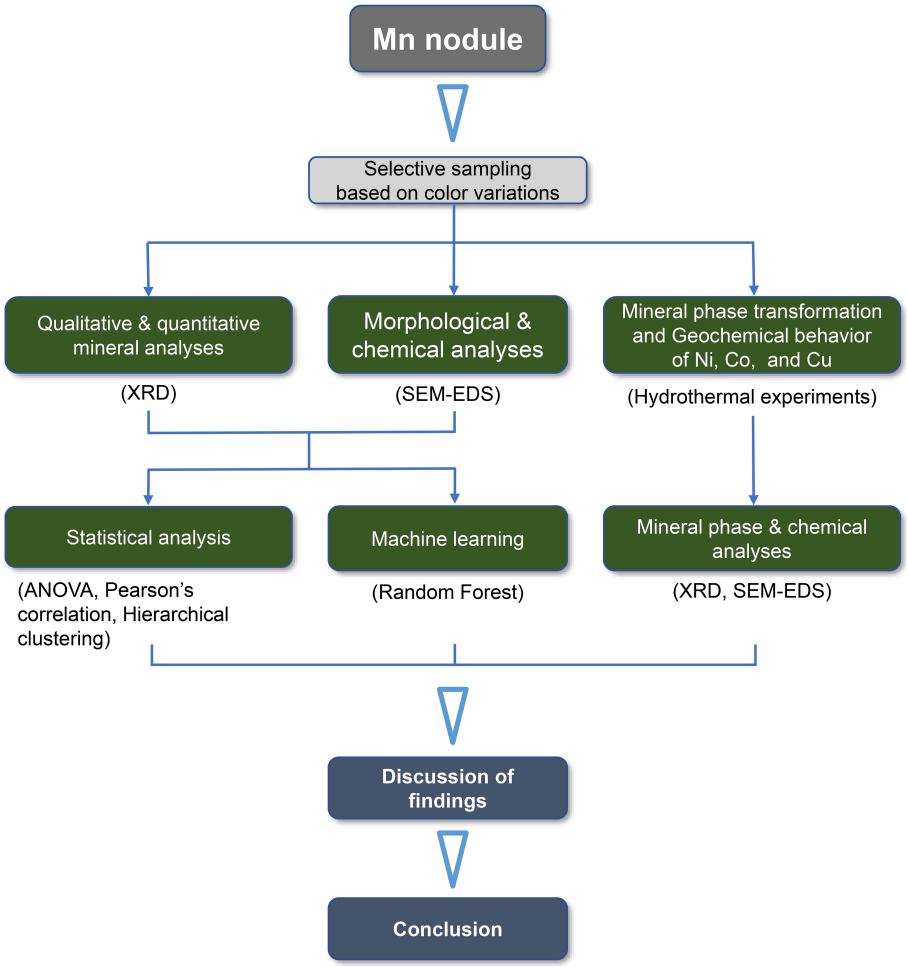

FIGURE 2
Workflow diagram of this study.

analysis also confirmed the presence of an elongated fibrous structure (Supplementary Figure S2). Therefore, the 10 Å peak observed after heating can be attributed to the Bragg peak of todorokite rather than thermally stable buserite II. The mineral phases of Mn nodules from KC-2 included vernadite, quartz, apatite, plagioclase, todorokite, and buserite (Figure 3A). KC-8 Mn nodules contained vernadite, quartz, plagioclase, apatite, goethite, todorokite, and buserite (Figure 3B). OSMxx Mn nodules exhibited vernadite, quartz, apatite, todorokite, goethite, and plagioclase (Figure 3C). The manganate minerals commonly identified in all three locations were vernadite and todorokite, while buserite was observed only in KC-2 and KC-8, and was absent in OSMxx. Regarding todorokite, although its content is not high (Supplementary Table S1), it is present in samples from all sites, indicating that the Mn nodules in the study area have undergone suboxic environmental conditions (Heller et al., 2018; Wegorzewski et al., 2020). Aside from manganate minerals, quartz and plagioclase were mainly derived from sediments (Jung et al., 2023). In the case of apatite, the apatite found in Mn nodules can be classified into bioapatite, which originates from fish bones (Huang et al., 2023), and carbonate fluorapatite (or fluorapatite), which is of inorganic origin (Jiang et al., 2020). These two types can be distinguished based on their morphological characteristics: bioapatite retains the shape of fish teeth, whereas carbonate fluorapatite occurs in a euhedral form, appearing as hexagonal plates or columns. Thus, the apatite found in Mn nodules from the study area should be identified based on its morphology using SEM analysis (as discussed in SEM analysis results). Goethite was observed in KC-8 and OSMxx, and in samples where goethite was confirmed, a weak peak was also observed near $2\theta = 36.2°$ (2.50 Å). Previous studies (Liu et al., 2021; Namgung and Lee, 2021; Liu et al., 2022; Tong et al., 2025) explained that Fe (oxyhydr)oxides, such as goethite, ferrihydrite, hematite, can adsorb Mn ions and promote their growth into Mn oxides. As well as Fe (oxyhydr)oxides, clay minerals, such as kaolinite and montmorillonite, can also adsorb Mn ions and advance their growth (Yang et al., 2023). However, the peak at 2.50 Å is presumed to correspond to ferrite with a spinel structure (discussed in the following section).

Concerning the morphological characteristics of Mn nodules, the representative SEM images of each sample exhibit the following features. In KC-2, angular Mn nodule particles are observed, including spherical Mn nodule particles with an average size of 100 µm (Figure 4A). A magnified view of the spherical Mn nodule

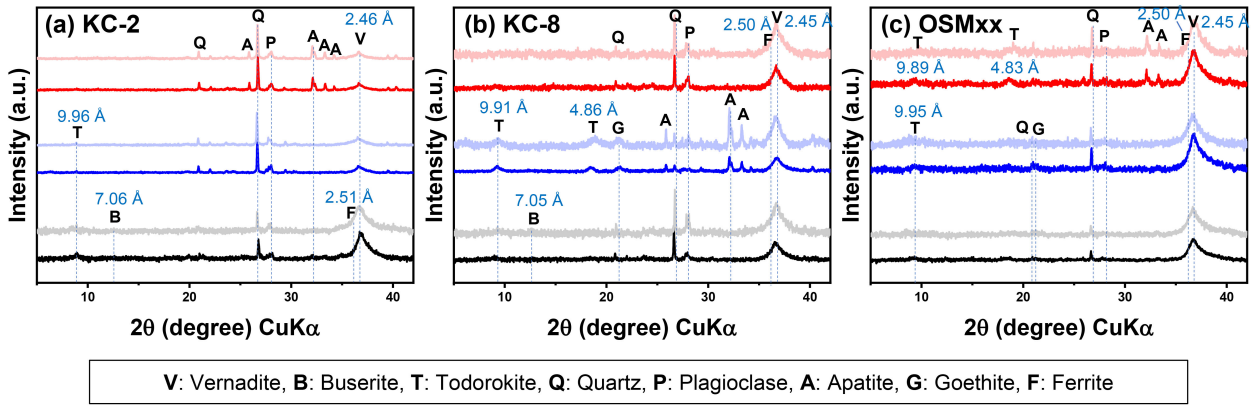

FIGURE 3
Representative XRD patterns (background subtracted) of three samples from each study area: (a) KC-2, (b) KC-8, and (c) OSMxx, shown before (bold) and after heating (light).

particles reveals that they are composed of layered structures with particles stacked in multiple layers (Figure 4B). In KC-8, the layered structure of Mn nodule particles, as observed in KC-2, is more distinctly visible (Figure 4C). In OSMxx, the presence of apatite within Mn nodule particles is confirmed (Figure 4D). Apatite exhibits a hexagonal morphology, with an average size of 2–3 µm, characteristic of carbonate fluorapatite, an inorganic mineral, as previously discussed (Jiang et al., 2020), suggesting that this carbonate fluorapatite preferentially forms under suboxic conditions. Although not all minerals identified through XRD analysis, such as carbonate fluorapatite, were directly observable, SEM images confirmed the presence of vernadite, characterized by a layered structure of stacked small particles. Additionally, the visible presence of carbonate fluorapatite further supports the conclusion that the Mn nodules formed under suboxic conditions.

The chemical composition results for all samples are presented in Supplementary Table S1. The major chemical elements show that the average Mn content in Mn nodules is 35.74 ± 14.98% for KC-2, 41.04 ± 4.13% for KC-8, and 48.67 ± 8.96% for OSMxx. In comparison, the average Fe content is 28.80 ± 5.43% for KC-2, 32.32 ± 2.82% for KC-8, and 23.44 ± 5.24% for OSMxx; Mn and Fe concentrations exhibit slight variations depending on the sampling location. Although the chemical compositions were averaged, the large deviation between the minimum and maximum values makes it difficult to fully capture the differences in chemical composition among the three regions based on average values alone. In particular, the high standard deviations observed at KC-2 indicate that its chemical compositions are more widely distributed from the mean, likely due to the influence of sediments. Although the dark regions of KC-2 were also sampled using a micro-drill, the relatively high sediment content (Supplementary Figure S1) suggests that some sediment material may have been incorporated into the samples. Therefore, ANOVA analysis was conducted to assess statistically significant differences among the three locations, and the results are visually represented in Supplementary Figure S3 for better understanding. The ANOVA analysis results indicate that the Mn and Fe contents in KC-2 and KC-8 are similar, whereas OSMxx exhibits a higher Mn content and a lower Fe content than the other two locations. The Si and Al contents are also lower in OSMxx than in the other two locations. In contrast, no significant differences among the three locations were observed for Mg, Ca, Na, K, Cl, P, S, and Ti. Regarding the primary elements of interest, Ni, Co, and Cu, the Ni content in OSMxx was slightly higher than in the other two locations, although the difference was not substantial. Meanwhile, Co and Cu did not show statistically significant differences among the three locations. Overall, the ANOVA results indicate that the chemical compositions of Mn nodules from the three locations are statistically similar, which may suggest that they formed under comparable deep-sea environmental conditions.

Origin of Mn nodule formation

Geochemical diagram related to the genetic origin of Mn nodules, based on their chemical compositions, are shown in Figure 5. The ternary diagram utilizing Mn, Fe, Ni, and Cu shows that most Mn nodules from KC-2, KC-8, and OSMxx are plotted in the hydrogenetic origin region. Some KC-2 samples plot outside the hydrogenetic origin region, which may be attributed to the influence of hydrothermal activity. In addition to these, the chemical compositions of core samples from nearby seamounts (KC-3 and KC-4) and the additionally collected Mn nodule samples (Supplementary Figure S4) indicate that some KC-2 samples and specific depths (KC-3: 14.5 cm and 20.4 cm, KC-4: 10.5 cm and 15.4 cm) of the nearby seamount cores exhibit signatures of hydrothermal origin (Supplementary Figure S5, Supplementary Table S2; these data were not used for the statistical and machine learning analyses). In a specific KC-2 Mn nodule (Figure 6), boundaries are slightly observed between the central and outer parts, with differences in morphology and color. The outer part is mainly composed of vernadite, quartz, and plagioclase. In contrast, the central part contains clay minerals such as smectite, illite, and chlorite, together with quartz, plagioclase, fluorapatite, hematite, and ferrite. Here, ferrite [DB Card No. of Crystallography Open

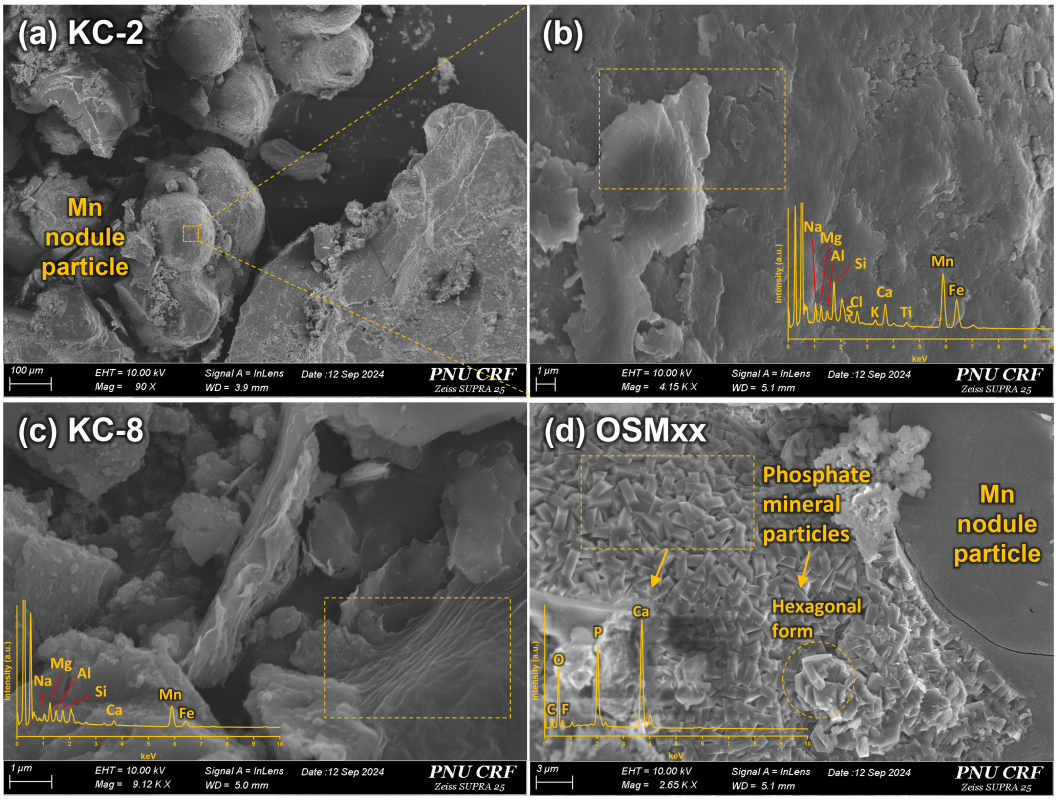

FIGURE 4
SEM–EDS analyses of representative samples: **(a, b)** KC-2, **(c)** KC-8, and **(d)** OSMxx.

Database (COD): 2300618] exhibits its two strongest reflections at 2.50 Å and 2.95 Å. Based on this, although the second strongest reflection at 2.95 Å is not clearly discernible in Figure 3 due to its low signal-to-noise (S/N) ratio, the 2.50 Å reflection is likely attributed to ferrite. Clay minerals can form either through hydrothermal alteration or through sedimentary input. The smectite observed in the central part is Fe–rich (Figures 7A, B). It is inferred to be nontronite, which likely formed through hydrothermal alteration of volcanic detritus (Xiang et al., 2024). However, since REY or isotopic analyses were not conducted in this study, the Fe–rich smectite cannot be conclusively identified as hydrothermal in origin. The ferrite with a spinel structure exists as nanosized particles, making it difficult to distinguish from hematite based solely on morphology (Figure 7C). However, it can be clearly differentiated in the XRD patterns (Figure 6). Such spinel–structured ferrite requires thermal energy for its formation. Therefore, the presence of ferrite and the origin of some KC-2 Mn nodules indicates that hydrothermal activity occurred during their formation. Moreover, the ANOVA results for KC-2 (Supplementary Figure S3) further show that Si and Al are more enriched and exhibit a broader concentration range than those in Mn nodules from the other two locations. This is likely attributed to the influence of sediments, including the aforementioned clay minerals.

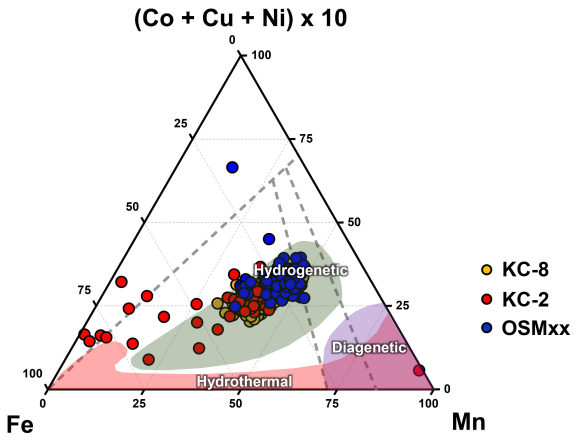

FIGURE 5
Geochemical diagram to distinguish the genetic origin of Mn nodules: Ternary diagram of 10*(Co + Cu + Ni)–Fe–Mn (adapted after Bonatti et al., 1972).

Most Mn nodules plot within the hydrogenetic origin region. While several KC-2 samples fall outside this region, the majority of Mn nodules from the three locations are primarily hydrogenetic and formed under oxic conditions. Compared with the mineral quantification results, the proportion of todorokites in the KC-2 samples is relatively higher than that at the other two locations (Supplementary Table S1). These todorokites can form in diagenetic conditions, including hydrothermal conditions (Atkins et al., 2014,

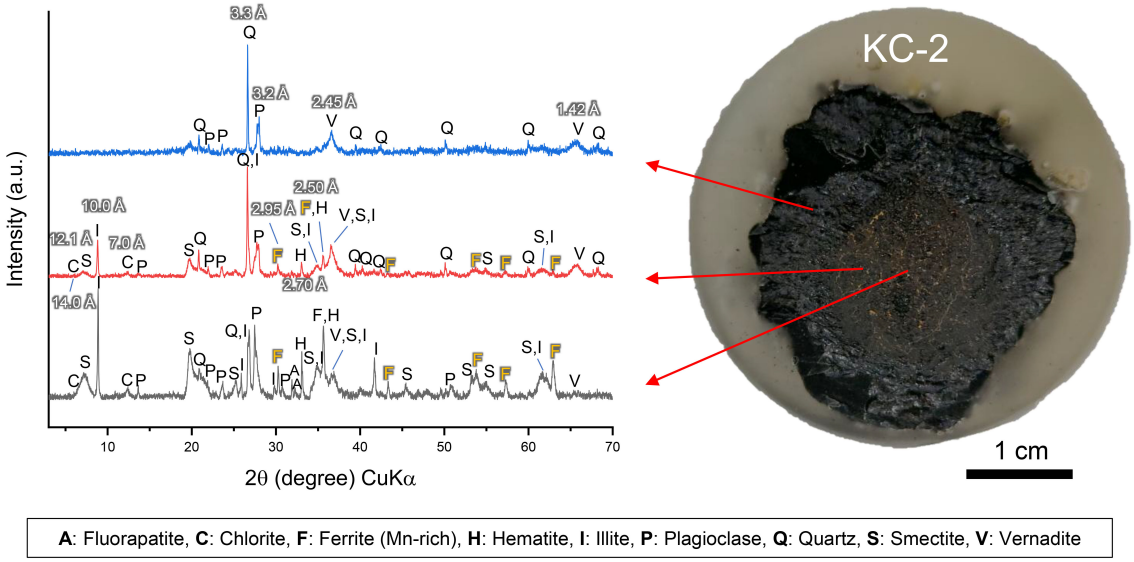

FIGURE 6
Background-subtracted XRD patterns of the central and outer parts of a specific KC-2 Mn nodule.

Atkins et al., 2016; Shi et al., 2024). In addition, the presence of carbonate fluorapatite across all study areas suggests that the Mn nodules have experienced diagenetic conditions (Jiang et al., 2020). Nevertheless, the geochemical diagram based on the nodules' chemical compositions still indicates a predominantly hydrogenetic origin. These results suggest that the nodules may have experienced transient changes (e.g., suboxic and hydrothermal fluids) in deep-sea environmental conditions over the long periods during which they grew.

Correlation between mineral phase and heavy metals

As determined through geochemical diagrams, the formation environment of Mn nodules predominantly corresponds to a hydrogenetic environment (Figure 5); however, some minerals, such as todorokite and carbonate fluorapatite, also indicate a diagenetic environment (Jiang et al., 2020; Wegorzewski et al., 2020). In this regard, Ni, Co, and Cu concentrations are generally similar across the three locations, except for Ni, which is relatively enriched only in OSMxx (Supplementary Figure S3). Similarly, the correlation between manganate minerals, such as todorokite, buserite, and vernadite, and heavy metals appears to be insignificant (Supplementary Figure S6). In fact, vernadite accounts for the majority (over 90%) of the manganate minerals in the Mn nodules collected from the three locations, making it difficult to establish correlations with heavy metals, which are present only in trace amounts (less than approximately 2%) (Supplementary Table S1). Therefore, despite their trace-level presence, basic statistical analyses and the machine learning algorithm Random Forest were employed as an attempt to investigate their correlation with manganate minerals.

Pearson correlation and hierarchical clustering analyses were conducted to examine the correlation between manganate minerals and their chemical compositions within Mn nodules, and the results are presented in Figure 8. In the Pearson correlation analysis, values with a p-value of ≤ 0.05 are numerically indicated. The hierarchical clustering technique was applied to analyze the correlations among variables, grouping highly correlated variables into the same cluster. The clustered results are highlighted with bold black rectangles, and the corresponding dendrogram is displayed on the right to visually represent the clustering structure. Interestingly, the correlations between the three manganate minerals and chemical compositions were clearly distinguished. Vernadite exhibited a positive correlation with Mn, and our primary target heavy metals—Ni, Co, and Cu—forming a distinct cluster. Buserite clustered with Na and Cl, showing a positive correlation, while it exhibited a negative correlation with Ca, S, and P. Lastly, todorokite demonstrated a negative correlation with Fe and V, whereas it clustered positively with Ti, Mg, K, Si, and Al (Figure 8). These results indicate that although Ni, Co, and Cu did not exhibit particularly strong positive correlations, they are still associated with vernadite. Specifically, in the clustering structure (dendrogram), Ni is paired with Mn, Co with vernadite, and Cu with Zn. Consquently, the results of Pearson correlation analysis and hierarchical clustering indicate that Ni, Co, and Cu exhibit a positive correlation with vernadite rather than with all three manganate minerals. However, the initial Random Forest predictive models for Ni, Co, and Cu, constructed using only the contents of the three manganate minerals, resulted in horizontally distributed data, indicating a failure to establish a valid model (Supplementary Figure S7). To improve model performance, additional mineralogical factors—specifically the FWHM and area of the XRD peaks for vernadite—were subsequently incorporated into the improved model, which enhanced the accuracy and reliability of the predictions.

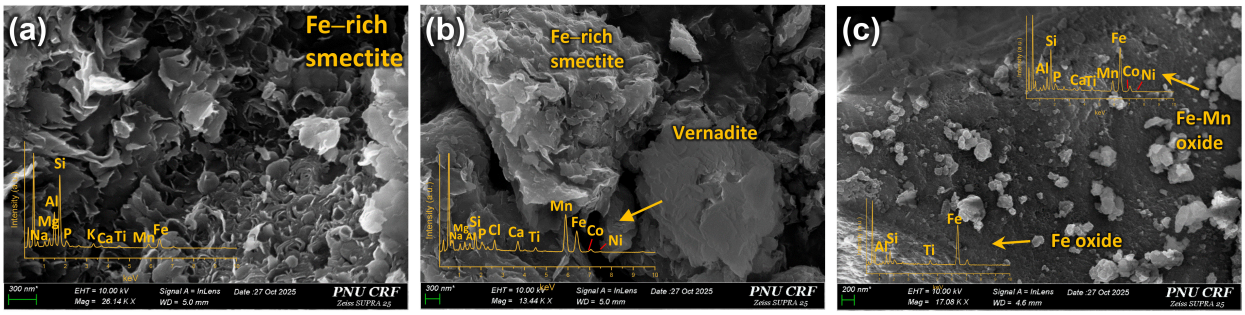

FIGURE 7
SEM-EDS analyses of Mn nodules from KC-2: **(a)** Fe–rich smectite, **(b)** Fe–rich smectite with vernadite, **(c)** Fe–(Mn) oxide.

The XRD peak corresponding to vernadite exhibited a broad width (Figure 3). To verify whether the broad and asymmetric peak corresponding to vernadite was influenced by other manganate minerals such as todorokite, heat treatment was conducted at 300°C (Wegorzewski et al., 2015) (Supplementary Figure S8). Although a small amount of todorokite is present, the broad and asymmetric peak of vernadite shows no significant change—that is no peak splitting occurs. Considering that the average content of todorokite in Mn nodules from the study area is relatively low (less than approximately 5%; Supplementary Table S1), the broad and asymmetric peak is attributed to the high degree of structural disorder in layered manganate minerals such as vernadite. Therefore, to achieve a high fitting accuracy ($R^2 > 0.9$), deconvolution was performed based on 2.45 Å ("Left") and 2.40 Å ("Right"); however, the 2.40 Å peak does not represent todorokite. The diagrams plotting the calculated FWHM values, peak areas, and heavy metal concentrations indicate no significant correlation (Supplementary Figure S9). This result suggests that a simple plot diagram alone is insufficient to confirm

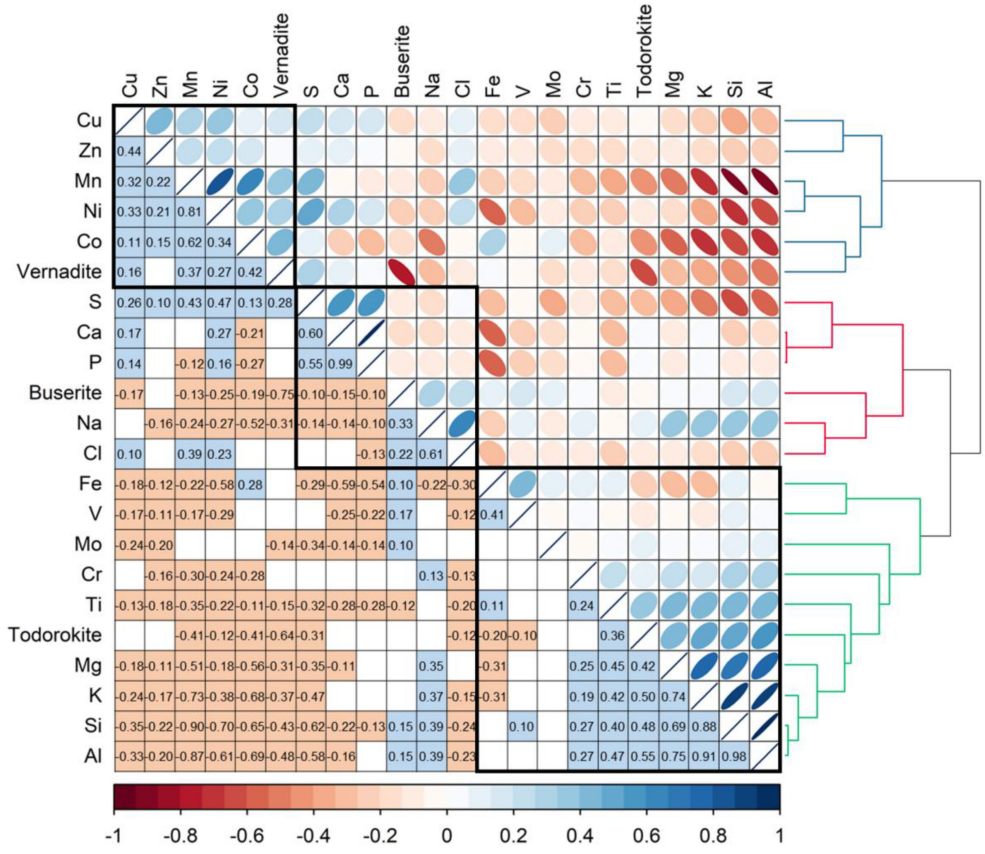

FIGURE 8
Pearson correlation and dendrogram (hierarchical clustering) results of chemical compositions and manganate minerals (todorokite, buserite, vernadite) in Mn nodules. Correlation coefficients are labeled only when the significance level is 0.05 or lower.

the positive correlation between vernadite and heavy metals observed in the statistical analysis (Figure 8). Therefore, a Random Forest machine learning analysis was performed again using these XRD peak parameters of vernadite as input variables. In Figure 9, the Random Forest predictive model, using the FWHM and area of the vernadite XRD peak as response variables, exhibits a linear relationship with the predictor variables Ni, Co, and Cu, indicating a strong correlation. For Ni (Figure 9A), the training model demonstrates excellent performance with an R^2 value of 0.92. Although the validation model has a slightly lower R^2 value of 0.83, it still provides a sufficiently good model fit. The test model also achieves a high R^2 value of 0.81, confirming that the Random Forest-based predictive model for Ni is highly applicable. In the case of Co (Figure 9B), the training, validation, and test models all exhibit R^2 values above 0.9, suggesting that the predictive model for Co is even more suitable than that for Ni. Lastly, for Cu (Figure 9C), the training model achieves a remarkably high R^2 value of 0.94, while the validation and test models have R^2 values of 0.81 and 0.82, respectively. These results indicate that the predictive model for Cu also performs well, demonstrating strong predictive capabilities.

Regarding the Random Forest results, the response variables used in the predictive model were four parameters: FWHM_Left, FWHM_Right, Area_Left, and Area_Right. Feature importance was evaluated to determine which factor significantly influenced the Random Forest predictive model (Supplementary Figure S10). The results indicate that for Ni and Co, FWHM_Right had the highest feature importance values of 0.835 and 1.313, respectively. In the case of Cu, Area_Left exhibited the highest feature importance value of 0.559, suggesting that it played the most significant role in the model. Through feature importance analysis, it was confirmed that Ni and Co are associated with the FWHM of the XRD peak (particularly Co), while Cu is related to the peak area. Interestingly, these findings align with the results from Pearson correlation and hierarchical clustering analyses (Figure 8), where vernadite and Co exhibited the highest correlation and were directly clustered together, followed by Ni. Cu, on the other hand, was primarily clustered with Zn, showing a slightly lower correlation with vernadite than Ni and Co. Consequently, the Random Forest results are consistent with the statistical analysis results, clearly demonstrating that among the manganate minerals, vernadite exhibits a positive correlation with heavy metals such as Ni, Co, and Cu. Moreover, it can be seen that statistical analyses and the machine learning algorithm are sufficient to investigate correlations with other factors, even for trace-level elements.

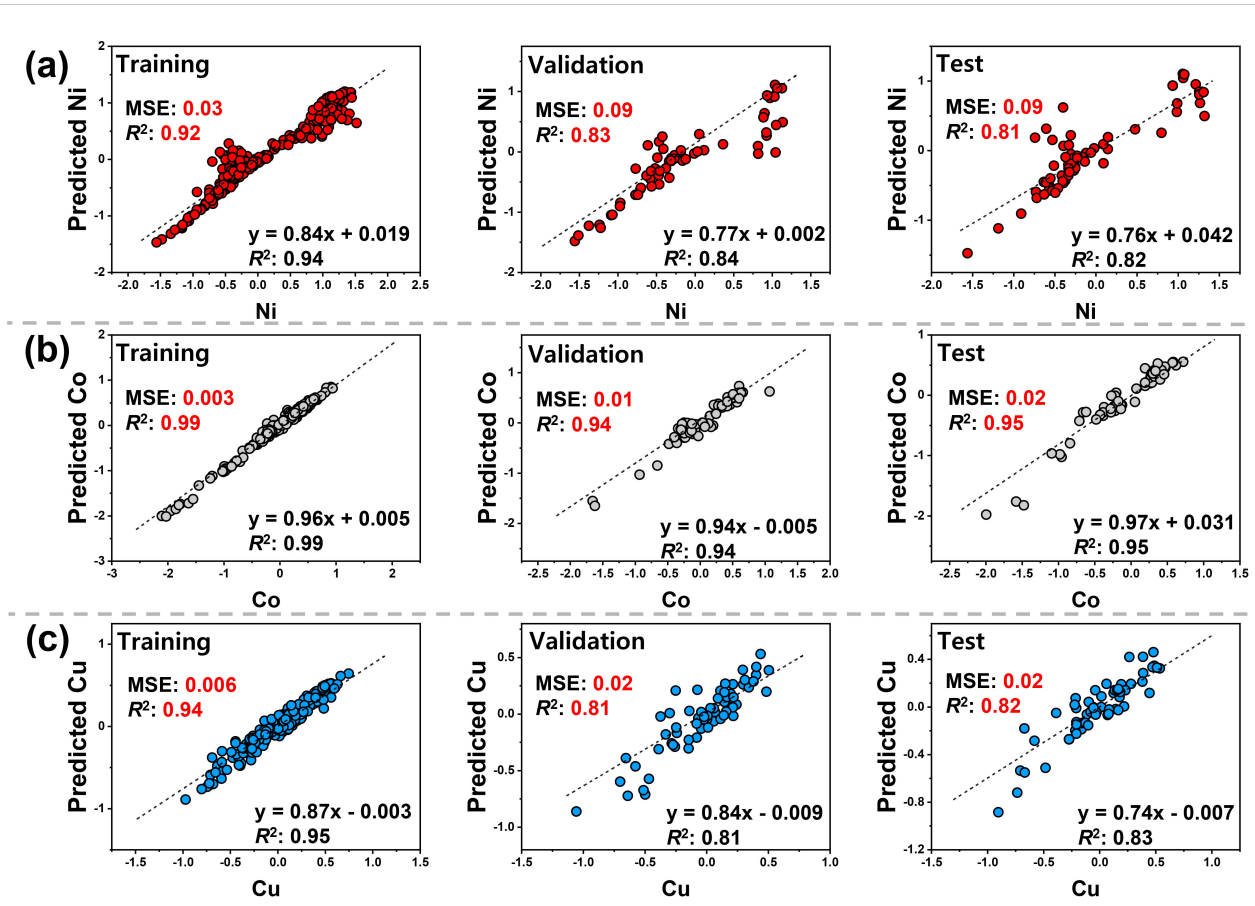

FIGURE 9
Random forest predictive models for significant economic elements: Ni **(a)**, Co **(b)**, and Cu **(c)**, based on standardized vernadite XRD peak properties (FWHM and area) and chemical compositions.

Geochemical behavior of heavy metals during mineral phase transformation

The Mn nodules collected from the KC-2, KC-8, and OSMxx study areas are primarily composed of the manganate mineral vernadite, with smaller amounts of todorokite and buserite (Figure 2). In addition, they contain various other minerals, including quartz, plagioclase, apatite, and goethite. Regarding these results, although the geochemical diagrams (Figure 5) indicate that most Mn nodules originate from a hydrogenetic environment, the mineral phases identified through XRD analysis suggest that they also reflect diagenetic environments (e.g., todorokite and apatite) (Atkins et al., 2014; Heller et al., 2018; Jiang et al., 2020; Wegorzewski et al., 2020). In other words, vernadite within Mn nodules may undergo mineral phase transformation in response to changes in deep-sea environmental conditions, which could alter the geochemical behavior of Ni, Co, and Cu incorporated within vernadite. For this reason, samples with high concentrations of these three heavy metals were selected, and mineral phase transformation experiments were conducted under oxic and suboxic conditions to clarify their geochemical behavior during the transformation process.

Under oxic conditions, little to no mineral phase transformation is observed with changes in pH (Figure 10A). From pH 7 to the alkaline condition of pH 12, variations in the XRD peak intensities of plagioclase and todorokite are observed; however, no significant mineral phase transformation occurs. In contrast, under suboxic conditions (Figure 10B), a noticeable increase in the XRD peak intensity of todorokite is observed at neutral pH 7, and newly formed minerals, including Ca–Fe–Mn phosphate, goethite, hematite, and Fe–Mn oxide minerals, begin to appear. The plagioclase peak is scarcely observed at pH 3 and pH 12. The newly formed Ca–Fe–Mn phosphate mineral and Fe–Mn oxide are considered to correspond to fluorapatite and manganese ferrite [Mn ferrite (spinel structure)], respectively, based on the XRD patterns (Mabilleau et al., 2010; Jiang et al., 2020; Akhlaghi and Najafpour-Darzi, 2021; Wen et al., 2023). The contrast between the mineral composition changes in Mn nodules under oxic and suboxic conditions is quite pronounced. This suggests that hydrogenetic Mn nodules, which typically form under oxic conditions, may undergo mineral phase transformation when subjected to suboxic diagenetic environments. Furthermore, the formation environment of Mn nodules can be inferred not only from geochemical diagrams based on chemical composition but also from XRD-based mineral identification.

In terms of mineral phase transformation conditions, the pH of seawater and sediment porewater is approximately 7–8 (Peacock, 2009; Peña et al., 2010; Sherman and Peacock, 2010), which is close to neutral. The experimental results under suboxic conditions (Figure 10B) also indicate that a phase transition of manganate minerals can occur at pH 7. Here, temperature is another key environmental factor influencing mineral phase transformation in deep-sea environments. Previous studies have reported that todorokite can be synthesized within a temperature range of approximately up to 160°C (Ching et al., 1999; Feng et al., 2004, 2010). Therefore, we conducted mineral phase transformation experiments under suboxic conditions at pH 7 by varying the temperature at 90, 120, and 150°C. As shown in Figure 10C, alterations in the intensity and shape of the plagioclase peak become noticeable at 90°C. At 120°C, fluorapatite begins to crystallize. At this temperature, a slight increase in peak intensity is observed at the main diffraction positions of goethite, hematite, and Mn ferrite, along with a subtle increase in both the intensity and FWHM of the todorokite peak. At 150°C, the peak intensities of newly formed minerals further increase relative to those at 120°C, while the diffraction intensities of plagioclase and quartz decrease significantly.

The presence of todorokite, fluorapatite, and Mn ferrite, formed under suboxic conditions, was further confirmed by SEM-EDS analysis (Figures 10D–F). Todorokite appears as elongated fibrous structures, with lengths ranging from approximately 20 nm to a maximum of 2 μm (Figure 10D). In the case of fluorapatite, although it does not exhibit a highly crystalline hexagonal shape, it forms an elongated structure ranging from 20 nm to 150 nm in length (Figure 10E). Lastly, Mn ferrite displays a well-crystallized spinel morphology, with particle sizes varying from approximately 100 nm to 500 nm (Figure 10F).

Additionally, SEM-EDS analysis confirmed the presence of Ni, Co, and Cu in todorokite, fluorapatite, and Mn ferrite (Figures 10D–F). Among these heavy metals, their relative concentrations in each mineral followed the order Co > Ni > Cu (Supplementary Table S3). These heavy metals can co-precipitate into the mineral structure of todorokite and spinel (Bodeï et al., 2007; Rosnan et al., 2016). Ni and Co can also be incorporated into the mineral structure of fluorapatite. According to a previous study (Mabilleau et al., 2010), the lattice parameter *c* of raw fluorapatite is approximately 7.232 Å; however, it decreases to below 7 Å when Ni and Co are co-precipitated. The XRD peaks of fluorapatite formed during the hydrothermal experiments exhibited low intensity, making it difficult to obtain precise lattice parameters through Rietveld refinement. Therefore, in this study, the Rietveld refinement was applied to identify the crystalline phase of fluorapatite and to semi-quantitatively estimate its lattice parameters. The obtained lattice parameters of fluorapatite are 9.415 Å for *a* and *b*, and 6.893 Å for *c*. Although the XRD peaks of fluorapatite are relatively weak and the precision of lattice parameter determination is limited, this approximate *c* value is lower than 7 Å.

Discussion

The results of the hydrothermal experiments (Figure 10; Supplementary Table S3) demonstrate that vernadite, the primary manganate mineral in Mn nodules, can undergo mineral phase transformation in response to changes in the deep-sea environment. In the phase transformation process of manganate minerals, Mn^{4+}, the main constituent of vernadite, can be partially reduced to soluble Mn^{2+} when exposed to suboxic conditions and hydrothermal fluids (Wegorzewski et al., 2020). The formation of

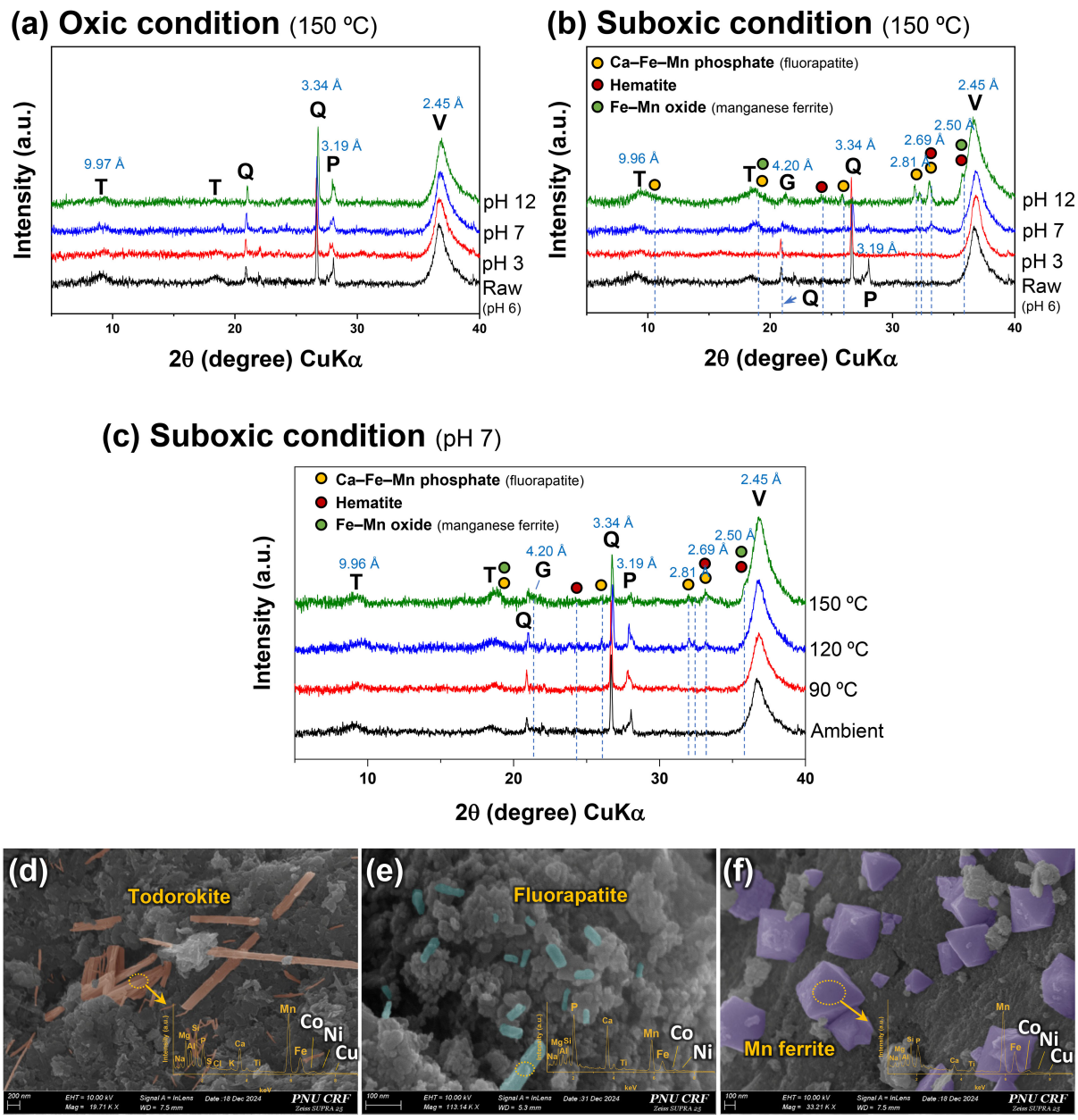

FIGURE 10
Changes in the mineral phases under oxic **(a)** and suboxic **(b)** conditions (temperature: 150°C, reaction time: 72 h), and suboxic conditions at different temperature **(c)** (pH: 7, reaction time: 72 h). SEM-EDS results for minerals: pseudo-colored todorokite **(d)**, fluorapatite **(e)**, and manganese ferrite **(f)**. T, todorokite; V, vernadite; Q, quartz; P, plagioclase; G, goethite.

Mn ferrite ($MnFe_2O_4$) observed in the hydrothermal experiments supports this phenomenon (Figures 10B, C, F). As Mn^{4+} is reduced to Mn^{2+} and partially dissolves, structural defects develop in vernadite. The dissolved Mn^{2+} ions can subsequently be readsorbed onto MnO_2 (vernadite), reacting with Mn^{4+} to generate oxidized Mn^{3+}, which may serve as a precursor for todorokite formation (Elzinga, 2016; Wegorzewski et al., 2020). After the hydrothermal experiments, the Mn nodule particles exhibited a significantly rough surface with small, detached fragments, suggesting that partial dissolution had occurred, resulting in the separation of small particles in a flake-like manner (Supplementary Figure S11). This phenomenon is considered a consequence of the partial dissolution caused by the reduction of Mn^{4+} to Mn^{2+}. However, unlike Mn^{4+}, Fe^{3+} is not readily reduced under suboxic or hydrothermal conditions. The formation of goethite (δ-FeOOH), hematite (Fe_2O_3), and Mn ferrite ($MnFe_2O_4$) in the hydrothermal experiments further supports this observation (Figures 10B, C, F).

Ni, Co, and Cu, which are either adsorbed onto the surface of vernadite or incorporated into its structure, exhibit altered geochemical behavior during the mineral phase transformation of Mn nodules. Previous studies have explained that vernadite of

hydrogenetic origin undergoes continuous dissolution under suboxic conditions as Mn^{4+} is reduced to Mn^{2+}, leading to the release of adsorbed or co-precipitated heavy metals into the porewater (Manceau et al., 2014). The heavy metals, such as Ni^{2+} and Co^{3+}, present in sediment porewater can then be re-adsorbed onto layered Mn oxide minerals such as vernadite or birnessite, where they integrate into the octahedral sheets. These minerals undergo a phase transformation into todorokite, incorporating the heavy metals into their structure in the process (Heller et al., 2018; Wegorzewski et al., 2020). Ni^{2+} and Cu^{2+} can also occupy the tunnels of todorokite as outer-sphere complexes (Atkins et al., 2016; Wegorzewski et al., 2020). Various experimental studies and analyses have provided evidence supporting the incorporation of Ni, Co, and Cu into the structure of manganate minerals (Atkins et al., 2016; Wu et al., 2019; Wegorzewski et al., 2020). However, most studies have primarily focused on the todorokite mineral under suboxic and hydrothermal conditions.

Our experimental results using natural Mn nodules demonstrate that Ni, Co, and Cu can be incorporated not only into todorokite but also into the phosphate mineral, fluorapatite, and the spinel-structured Mn ferrite (Figure 10; Supplementary Table S3). As mentioned in the previous chapter, Ni^{2+} and Co^{2+} can partially substitute Ca^{2+} at the (002) plane of fluorapatite (Mabilleau et al., 2010). In the case of Mn ferrite, Mn^{2+} can be substituted by Ni^{2+}, Co^{2+}, and Cu^{2+} (Chandra Sekhar et al., 2016; Rosnan et al., 2016). An interesting finding is that, although Mn ferrite is typically reported to form at high temperatures above 600°C in synthetic experiments (Rosnan et al., 2016; Yu et al., 2016; Ye et al., 2021; Wen et al., 2023), it was observed in our hydrothermal experiments even at relatively low temperatures (below 150°C). In addition to the experimental results, a weak diffraction peak corresponding to Fe–Mn oxides with a *d*-spacing of 2.50–2.51 Å was observed in the XRD patterns of Mn nodules from the study area (Figure 3). This reflection corresponds to either Mn ferrite or hematite (Figure 6). However, hematite typically exhibits its strongest peak at 2.70 Å; most samples could not show a distinct hematite peak. Therefore, although KC-8 and OSMxx do not exhibit as clear evidence of Mn ferrite as KC-2, the weak Fe–Mn oxide peak observed at 2.50–2.51 Å is presumed to correspond to Mn ferrite. These results suggest that Mn ferrite can form under actual deep-sea environments with relatively low-temperature and suboxic conditions. In general, deep-sea Mn nodules grow through alternating exposure to oxic and suboxic conditions (Kuhn et al., 2017a). Moreover, the deep-sea environment in which Mn nodules formed is likely a transition zone with alternating oxic and suboxic conditions. Therefore, the presence of todorokite, fluorapatite, and Mn ferrite in KC-2, KC-8, and OSMxx indicates that Mn nodules in these regions have experienced both oxic and suboxic conditions during their formation.

In more detail regarding the environmental characteristics, the mineral phase of Mn nodules from the KC-2 includes todorokite and fluorapatite (Figure 3), suggesting exposure to suboxic conditions at temperatures between 120°C and 150°C. In contrast, Mn nodules from KC-8 and OSMxx contain not only todorokite and fluorapatite but also Mn ferrite (Figure 3), suggesting that these nodules experienced suboxic conditions at temperatures exceeding 150°C. Although it is difficult to determine the extent to which Mn nodules have been exposed to oxic and suboxic conditions, mineral phase changes imply their potential as key indicators for inferring deep-sea environmental conditions. Regarding deep-sea environment changes, the Magellan Seamounts are inferred to have been affected by phosphatization events as well as hydrothermal fluid activity. According to a recent study (Li et al., 2023), the mineralogical and geochemical characteristics of manganese crust and substrate rock samples collected from the Magellan Seamounts revealed the presence of ferromanganese particles formed by hydrothermal activity. In particular, the reaction interface of the hydrothermally derived ferromanganese particles showed a clear reaction interface with portions formed by hydrogenetic and phosphatization processes. This hydrothermal activity in the Magellan Seamounts is presumed to be the primary cause for the formation of the minerals Mn ferrite (Fe–Mn oxide), todorokite, and CFA identified in our Mn nodule samples (Figure 3). Concerning the hydrothermal temperature, a previous study (Bau, 1991) reported that a positive Eu anomaly occurs at temperatures above 200°C because Eu^{3+} in rocks is reduced to the more soluble Eu^{2+}. Therefore, if a positive Eu anomaly is not observed in the Mn nodules from the study area, it suggests that the hydrothermal temperature is below 200°C. Although we confirmed hydrothermal activity in the Magellan Seamounts through the mineral phases in Mn nodules and a previous study (Li et al., 2023), we were unable to present the hydrothermal temperature due to the absence of Eu element analysis in our study. To address this issue, we plan to analyze the REE concentrations, including Eu, in Mn nodule and Mn crust samples to be collected during future expeditions in order to present a more precise hydrothermal temperature.

The Mn nodule samples we collected are predominantly composed of the turbostratic phyllomanganate mineral vernadite. This vernadite primarily forms under oxic hydrogenetic conditions and adsorbs various heavy metals, including Ni, Co, and Cu. When Mn nodules dominated by vernadite are exposed to diagenetic environments, including suboxic hydrothermal fluids, the reduction of Mn within vernadite leads to partial dissolution and structural defects, initiating mineral phase transformation. As a result, vernadite undergoes transformation into more stable minerals suited to the exposed conditions, such as tunnel-structured todorokite, fluorapatite, and Mn ferrite, with heavy metals becoming co-precipitated into their mineral structures (Figure 11). The concentrations of trace metals in todorokite, fluorapatite, and Mn ferrite identified in the hydrothermal experiments differ (Supplementary Table S3). However, since the total concentrations of trace metals do not change during hydrothermal experiments, these variations are likely due to differences in selectivity between minerals and trace metals rather than an environmental difference. The selectivity (K_d) of heavy metals for these minerals could not be clearly determined due to their trace concentrations in the Mn nodules and the extremely small particle sizes of the newly formed minerals, which made precise analysis difficult. Nevertheless, these mineral phase transformations, along with their associated deep-sea

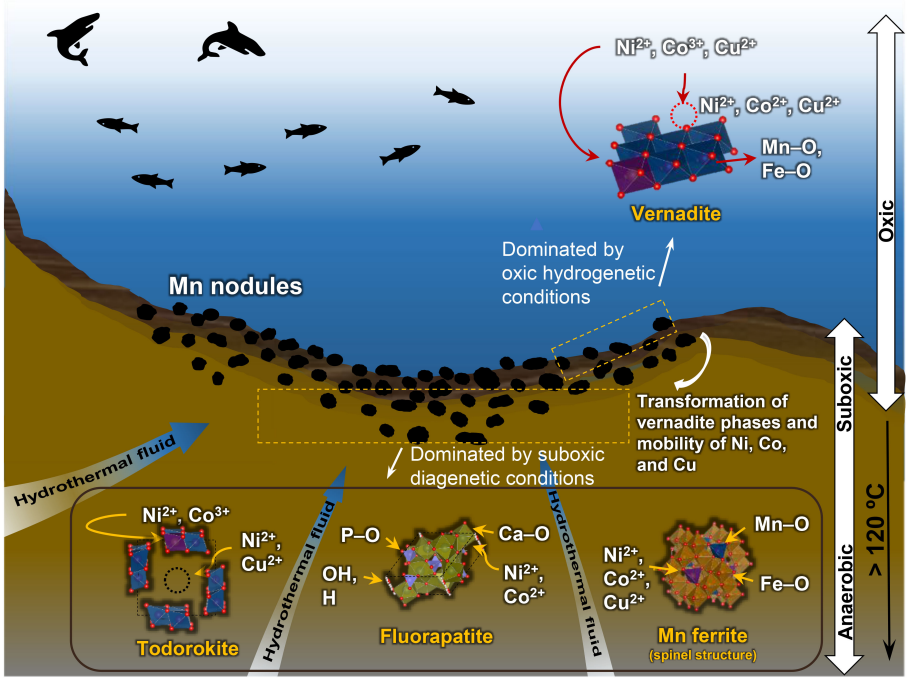

FIGURE 11
Schematic diagram illustrating changes in mineral phases of Mn nodules and the behavior of Ni, Co, and Cu under deep-sea environmental conditions.

environments and the geochemical behavior of heavy metals, are expected to contribute to a better understanding of Mn nodules. Additionally, to better understand the correlation between the differences in heavy metal concentrations associated with environmental changes (hydrogenetic and diagenetic) and the distribution of mineral phases, a comparison with Mn nodule samples from areas with distinct environmental conditions, such as the Clarion-Clipperton Zone (CCZ), will be required.

In conclusion, we investigated the correlation between manganate minerals and Ni, Co, and Cu, and examined the deep-sea formation environment and the geochemical behavior of these heavy metals by integrating statistical and machine learning analyses with actual Mn nodule experiments. To date, most studies utilizing machine learning in Mn nodule research have focused on developing predictive models to estimate the distribution of Mn nodules (Gazis et al., 2018; Hong et al., 2022; Josso et al., 2023). Moreover, our previous study (Jung et al., 2023) did not establish the relationships among minerals, elements, and deep-sea environmental conditions, primarily because of an insufficient number of samples, which limited the availability of comprehensive data. In contrast, our study uniquely applied machine learning to establish correlations between mineral phases and chemical compositions. The integration of basic statistical analysis and machine learning techniques proved highly valuable, enabling correlation inference based solely on XRD and SEM-EDS analyses of Mn nodules. However, a limitation of this study is that the Mn nodules collected from the study area predominantly contain vernadite, making it difficult to clearly identify correlations between other manganate minerals, such as buserite or todorokite, and heavy metals. Although the statistical analysis results (Figure 8) indicate that not all heavy metals are associated with vernadite, the limited diversity of mineral phases has hindered further correlation analysis. Therefore, to supplement these findings and enhance the reliability of the correlations, it is necessary to obtain Mn nodules with higher contents of other manganate minerals, such as todorokite or buserite, and to conduct statistical and machine learning analyses using data acquired through the same methodology. Certain Mn nodules collected from other regions have been confirmed to contain high concentrations of these minerals. For instance, we additionally analyzed one Mn nodule collected from the CCZ, which is expected to have a different geological setting from the Magellan Seamounts in the Western Pacific, and found that it contains higher proportions of manganate minerals other than vernadite (in preparation). Thus, in our upcoming expedition, we plan to collect not only a greater number of Mn nodules but also Mn crust core samples, and to analyze the chemical composition of the collected samples using more precise methods such as XRF or LA-ICP-MS. This will help reduce potential data bias caused by the dominance of vernadite and provide more robust and clearer correlations.

Conclusion

The Mn nodules collected from the KC-2, KC-8, and OSMxx locations of the Magellan Seamounts in the Western Pacific are

predominantly composed of the manganate mineral vernadite in all three regions, with smaller amounts of todorokite and buserite. Additionally, quartz, plagioclase, and apatite are observed in the KC-2, while quartz, plagioclase, goethite, apatite, and Mn ferrite are present along with the manganate minerals in the KC-8 and OSMxx. The chemical composition distribution of Mn nodules from the three regions, identified through statistical analyses, shows some variations but is largely similar. Statistical and clustering analyses confirmed that Ni, Co, and Cu in Mn nodules are positively correlated with vernadite among the manganate minerals. This correlation between vernadite and these heavy metals was further validated using the Random Forest machine learning algorithm, demonstrating high predictive accuracy and reinforcing their strong association. Based on these findings, hydrothermal experiments were conducted using actual Mn nodules. Under oxic conditions, minimal to no mineral transformation was observed. In contrast, under suboxic conditions, new minerals such as todorokite, goethite, hematite, fluorapatite, and Mn ferrite formed, confirming that mineral phase transformation actively occurs within Mn nodules. Furthermore, Ni, Co, and Cu were found to be co-precipitated within the structures of todorokite, fluorapatite, and Mn ferrite, respectively, during mineral phase transformation. Therefore, the mineral phases of Mn nodules serve as key indicators for understanding both their formation environment and the geochemical behavior of heavy metals such as Ni, Co, and Cu. However, as mentioned in the Discussion chapter, it was challenging to thoroughly identify the correlations between other manganate minerals and heavy metals, as vernadite predominated among the manganate minerals in the Mn nodules. Accordingly, we plan to expand our research by incorporating additional Mn nodules and Mn crust samples collected during an upcoming expedition. Preliminary surveys have revealed that some Mn nodules contain higher proportions of other manganate minerals, such as todorokite and buserite, which are expected to yield more insightful results. Furthermore, beyond merely constructing predictive models, we propose an alternative approach to machine learning—one that focuses on understanding the correlations among materials based on model performance. We hope this perspective will facilitate broader applications in future studies across multiple disciplines.

Data availability statement

The original contributions presented in the study are included in the article/Supplementary Material, further inquiries can be directed to the corresponding author/s.

Author contributions

SK: Conceptualization, Investigation, Methodology, Visualization, Writing – original draft, Writing – review & editing. EJ: Formal Analysis, Investigation, Writing – original draft, Writing – review & editing. JK: Formal Analysis, Investigation, Writing – review & editing. DS: Methodology, Supervision, Writing – review & editing. KY: Methodology, Writing – review & editing. JJ: Methodology, Writing – review & editing. YK: Methodology, Writing – review & editing. YL: Conceptualization, Methodology, Supervision, Writing – review & editing.

Funding

The author(s) declare that financial support was received for the research and/or publication of this article. This research was funded by the National Research Foundation (NRF) of the Ministry of Science and ICT of Korean Government, grant numbers (RS-2023–00213761 and RS-2023-00284250); Global - Learning & Academic research institution for Master's·PhD students, and Postdocs (LAMP) Program of the National Research Foundation of Korea (NRF) grant funded by the Ministry of Education (RS-2023-00301938); the Korea Institute of Marine Science & Technology Promotion (KIMST), funded by the Ministry of Oceans and Fisheries (No. 20220509).

Conflict of interest

The authors declare that the research was conducted in the absence of any commercial or financial relationships that could be construed as a potential conflict of interest.

Generative AI statement

The author(s) declare that no Generative AI was used in the creation of this manuscript.

Any alternative text (alt text) provided alongside figures in this article has been generated by Frontiers with the support of artificial intelligence and reasonable efforts have been made to ensure accuracy, including review by the authors wherever possible. If you identify any issues, please contact us.

Publisher's note

Supplementary material

The Supplementary Material for this article can be found online at: https://www.frontiersin.org/articles/10.3389/fmars.2025.1707329/full#supplementary-material

References

Akhlaghi, N., and Najafpour-Darzi, G. (2021). Manganese ferrite (MnFe2O4) Nanoparticles: From synthesis to application -A review. *J. Ind. Eng. Chem.* 103, 292–304. doi: 10.1016/j.jiec.2021.07.043

Atkins, A. L., Shaw, S., and Peacock, C. L. (2014). Nucleation and growth of todorokite from birnessite: Implications for trace-metal cycling in marine sediments. *Geochim. Cosmochim. Acta* 144, 109–125. doi: 10.1016/j.gca.2014.08.014

Atkins, A. L., Shaw, S., and Peacock, C. L. (2016). Release of Ni from birnessite during transformation of birnessite to todorokite: Implications for Ni cycling in marine sediments. *Geochim. Cosmochim. Acta* 189, 158–183. doi: 10.1016/j.gca.2016.06.007

Bau, M. (1991). Rare-earth element mobility during hydrothermal and metamorphic fluid-rock interaction and the significance of the oxidation state of europium. *Chem. Geol.* 93, 219–230. doi: 10.1016/0009-2541(91)90115-8

Bish, D. L., and Post, J. E. (1989). Thermal behavior of complex, tunnel-structure manganese oxides. *Am. Mineral.* 74, 177–186.

Bodeï, S., Manceau, A., Geoffroy, N., Baronnet, A., and Buatier, M. (2007). Formation of todorokite from vernadite in Ni-rich hemipelagic sediments. *Geochim. Cosmochim. Acta* 71, 5698–5716. doi: 10.1016/j.gca.2007.07.020

Bonatti, E., Kraemer, T., and Rydell, H. (1972). "Classification and genesis of submarine iron-manganese deposits," in *Ferromanganese deposits of the Ocean Floor* (Springer, Berlin, Germany), 149–166.

Breiman, L. (2001). Random forests. *Mach. Learn.* 45, 5–32. doi: 10.1023/A:1010933404324

Calvo, G., and Valero, A. (2022). Strategic mineral resources: Availability and future estimations for the renewable energy sector. *Environ. Dev.* 41, 100640. doi: 10.1016/j.envdev.2021.100640

Chandra Sekhar, B., Rao, G. S. N., Caltun, O. F., Dhana Lakshmi, B., Parvatheeswara Rao, B., and Subba Rao, P. S. V. (2016). Magnetic and magnetostrictive properties of Cu substituted Co-ferrites. *J. Magnet. Magnetic Mater.* 398, 59–63. doi: 10.1016/j.jmmm.2015.09.028

Ching, S., Krukowska, K. S., and Suib, S. L. (1999). A new synthetic route to todorokite-type manganese oxides. *Inorganica Chimica Acta* 294, 123–132. doi: 10.1016/S0020-1693(99)00208-X

Cutler, D. R., Edwards, T. C. Jr., Beard, K. H., Cutler, A., Hess, K. T., Gibson, J., et al. (2007). Random forests for classification in ecology. *Ecology* 88, 2783–2792. doi: 10.1890/07-0539.1

Elzinga, E. J. (2016). 54Mn radiotracers demonstrate continuous dissolution and reprecipitation of vernadite (δ-mnO2) during interaction with aqueous mn(II). *Environ. Sci. Technol.* 50, 8670–8677. doi: 10.1021/acs.est.6b02874

Feng, X. H., Tan, W. F., Liu, F., Wang, J. B., and Ruan, H. D. (2004). Synthesis of todorokite at atmospheric pressure. *Chem. Mater.* 16, 4330–4336. doi: 10.1021/cm0499545

Feng, X. H., Zhu, M., Ginder-Vogel, M., Ni, C., Parikh, S. J., and Sparks, D. L. (2010). Formation of nano-crystalline todorokite from biogenic Mn oxides. *Geochim. Cosmochim. Acta* 74, 3232–3245. doi: 10.1016/j.gca.2010.03.005

Gazis, I.-Z., and Greinert, J. (2021). Importance of spatial autocorrelation in machine learning modeling of polymetallic nodules, model uncertainty and transferability at local scale. *Minerals* 11, 1172. doi: 10.3390/min11111172

Gazis, I. Z., Schoening, T., Alevizos, E., and Greinert, J. (2018). Quantitative mapping and predictive modeling of Mn nodules' distribution from hydroacoustic and optical AUV data linked by random forests machine learning. *Biogeosciences* 15, 7347–7377. doi: 10.5194/bg-15-7347-2018

Glasby, G. P., Ren, X., Shi, X., and Pulyaeva, I. A. (2007). Co–rich Mn crusts from the Magellan Seamount cluster: the long journey through time. *Geo-Marine Lett.* 27, 315–323. doi: 10.1007/s00367-007-0055-5

González, F. J., Somoza, L., Hein, J. R., Medialdea, T., León, R., Urgorri, V., et al. (2016). Phosphorites, Co-rich Mn nodules, and Fe-Mn crusts from Galicia Bank, NE Atlantic: Reflections of Cenozoic tectonics and paleoceanography. *Geochem. Geophys. Geosys.* 17, 346–374. doi: 10.1002/2015GC005861

Hein, J. R., Koschinsky, A., Bau, M., Manheim, F. T., Kang, J.-K., and Roberts, L. (2000). "Cobalt-rich ferromanganese crusts in the Pacific," in *Handbook of marine mineral deposits*. Ed. D. S. Cronan(Boca Raton, FL: Routledge), 239–279.

Hein, J. R., Mizell, K., Koschinsky, A., and Conrad, T. A. (2013). Deep-ocean mineral deposits as a source of critical metals for high- and green-technology applications: Comparison with land-based resources. *Ore Geol. Rev.* 51, 1–14. doi: 10.1016/j.oregeorev.2012.12.001

Heller, C., Kuhn, T., Versteegh, G. J. M., Wegorzewski, A. V., and Kasten, S. (2018). The geochemical behavior of metals during early diagenetic alteration of buried manganese nodules. *Deep Sea Res. Part I: Oceanog. Res. Papers* 142, 16–33. doi: 10.1016/j.dsr.2018.09.008

Hong, F., Huang, M., Feng, H., Liu, C., Yang, Y., Hu, B., et al. (2022). First demonstration of recognition of manganese crust by deep-learning networks with a parametric acoustic probe. *Minerals* 12, 249. doi: 10.3390/min12020249

Huang, F., Fu, Y., Li, D., Peng, J., He, W., Li, S., et al. (2023). Early diagenetic REE migration from Fe-Mn nodules to fish teeth in deep sea sediments. *Ore Geol. Rev.* 160, 105581. doi: 10.1016/j.oregeorev.2023.105581

Jiang, X. D., Sun, X. M., Chou, Y. M., Hein, J. R., He, G. W., Fu, Y., et al. (2020). Geochemistry and origins of carbonate fluorapatite in seamount FeMn crusts from the Pacific Ocean. *Mar. Geol.* 423, 106135. doi: 10.1016/j.margeo.2020.106135

Josso, P., Hall, A., Williams, C., Le Bas, T., Lusty, P., and Murton, B. (2023). Application of random-forest machine learning algorithm for mineral predictive mapping of Fe-Mn crusts in the World Ocean. *Ore Geol. Rev.* 162, 105671. doi: 10.1016/j.oregeorev.2023.105671

Jung, E., Park, S., Kim, H., and Han, S. (2024). Spatiotemporal variation in methylmercury and related water quality variables in a temperate river under highly dynamic hydrologic conditions. *Sci. Total Environ.* 932, 173090. doi: 10.1016/j.scitotenv.2024.173090

Jung, J., Lee, S., Yang, K., Kim, J., Hyeong, K., Ko, Y., et al. (2023). Semi-quantitative analyses of ferromanganese nodules from the pacific ocean using synchrotron X-ray powder diffraction. *Minerals* 13, 1555. doi: 10.3390/min13121555

Koppers, A. A. P., Staudigel, H., Wijbrans, J. R., and Pringle, M. S. (1998). The Magellan seamount trail: implications for Cretaceous hotspot volcanism and absolute Pacific plate motion. *Earth Planet. Sci. Lett.* 163, 53–68. doi: 10.1016/S0012-821X(98)00175-7

Kuhn, T., Versteegh, G. J. M., Villinger, H., Dohrmann, I., Heller, C., Koschinsky, A., et al. (2017a). Widespread seawater circulation in 18–22 Ma oceanic crust: Impact on heat flow and sediment geochemistry. *Geology* 45, 799–802. doi: 10.1130/G39091.1

Kuhn, T., Wegorzewski, A., Rühlemann, C., and Vink, A. (2017b). "Composition, formation, and occurrence of polymetallic nodules," in *Deep-Sea Mining: Resource Potential, Technical and Environmental Considerations*. Ed. R. Sharma (Cham, Switzerland (Springer): Springer International Publishing), 23–63.

Li, Z., Guo, Z., Li, D., Sun, X., Fu, Y., and He, G. (2023). Element migration of ferromanganese crust on the Western Pacific MC Seamount: Insights from LA-ICP-MS mapping analysis. *Ore Geol. Rev.* 159, 105543. doi: 10.1016/j.oregeorev.2023.105543

Liu, J., Chen, Q., Yang, Y., Wei, H., Laipan, M., Zhu, R., et al. (2022). Coupled redox cycling of Fe and Mn in the environment: The complex interplay of solution species with Fe– and Mn–(oxyhydr)oxide crystallization and transformation. *Earth-Sci. Rev.* 232, 104105. doi: 10.1016/j.earscirev.2022.104105

Liu, J., Inoué, S., Zhu, R., He, H., and Hochella, M. F. (2021). Facet-specific oxidation of Mn(II) and heterogeneous growth of manganese (oxyhydr)oxides on hematite nanoparticles. *Geochim. Cosmochim. Acta* 307, 151–167. doi: 10.1016/j.gca.2021.05.043

Mabilleau, G., Filmon, R., Petrov, P. K., Baslé, M. F., Sabokbar, A., and Chappard, D. (2010). Cobalt, chromium and nickel affect hydroxyapatite crystal growth *in vitro*. *Acta Biomater.* 6, 1555–1560. doi: 10.1016/j.actbio.2009.10.035

Manceau, A., Lanson, M., and Takahashi, Y. (2014). Mineralogy and crystal chemistry of Mn, Fe, Co, Ni, and Cu in a deep-sea Pacific polymetallic nodule. *American Mineralogist.* 99, 2068–2083. doi: 10.2138/am-2014-4742

Namgung, S., Guo, B., Sasaki, K., Lee, S. S., and Lee, G. (2020). Macroscopic and microscopic behaviors of Mn(II) (ad)sorption to goethite with the effects of dissolved carbonates under anoxic conditions. *Geochim. Cosmochim. Acta* 277, 300–319. doi: 10.1016/j.gca.2020.03.036

Namgung, S., and Lee, G. (2021). Rhodochrosite oxidation by dissolved oxygen and the formation of mn oxide product: the impact of goethite as a foreign solid substrate. *Environ. Sci. Technol.* 55, 14436–14444. doi: 10.1021/acs.est.1c02285

Peacock, C. L. (2009). Physiochemical controls on the crystal-chemistry of Ni in birnessite: Genetic implications for ferromanganese precipitates. *Geochim. Cosmochim. Acta* 73, 3568–3578. doi: 10.1016/j.gca.2009.03.020

Peña, J., Kwon, K. D., Refson, K., Bargar, J. R., and Sposito, G. (2010). Mechanisms of nickel sorption by a bacteriogenic birnessite. *Geochim. Cosmochim. Acta* 74, 3076–3089. doi: 10.1016/j.gca.2010.02.035

Post, J. E. (1999). Manganese oxide minerals: Crystal structures and economic and environmental significance. *Proc. Natl. Acad. Sci.* 96, 3447–3454. doi: 10.1073/pnas.96.7.3447

Rosnan, R. M., Othaman, Z., Hussin, R., Ati, A. A., Samavati, A., Dabagh, S., et al. (2016). Effects of Mg substitution on the structural and magnetic properties of Co0.5Ni0.5–x MgxFe2O4 nanoparticle ferrites. *Chin. Phys. B* 25, 047501. doi: 10.1088/1674-1056/25/4/047501

Sherman, D. M., and Peacock, C. L. (2010). Surface complexation of Cu on birnessite (δ-MnO2): Controls on Cu in the deep ocean. *Geochim. Cosmochim. Acta* 74, 6721–6730. doi: 10.1016/j.gca.2010.08.042

Shi, M., Li, Q., Wang, Q., Yan, X., Li, B., Feng, L., et al. (2024). A review on the transformation of birnessite in the environment: Implication for the stabilization of heavy metals. *J. Environ. Sci.* 139, 496–515. doi: 10.1016/j.jes.2023.06.019

Staudigel, H., Park, K. H., Pringle, M., Rubenstone, J. L., Smith, W. H. F., and Zindler, A. (1991). The longevity of the South Pacific isotopic and thermal anomaly. *Earth Planet. Sci. Lett.* 102, 24–44. doi: 10.1016/0012-821X(91)90015-A

Tong, S., Wei, H., Zhou, J., Yang, Y., Zhu, R., Chen, Q., et al. (2025). Atomic insights into the heterogeneous crystallization of manganese (oxyhydr)oxides on typical iron (oxyhydr)oxides: from adsorption to oxidation to crystallization. *Environ. Sci. Technol.* 59, 3961–3971. doi: 10.1021/acs.est.4c10093

Uspenskaya, T. Y., Gorshkov, A. I., and Sivtsov, A. V. (1987). Mineralogy and internal structure of Fe–Mn nodules from the Clarion-Clipperton Fracture Zone. *Int. Geol. Rev.* 29, 363–371. doi: 10.1080/00206818709466153

Vereshchagin, O. S., Perova, E. N., Brusnitsyn, A. I., Ershova, V. B., Khudoley, A. K., Shilovskikh, V. V., et al. (2019). Ferro-manganese nodules from the Kara Sea: Mineralogy, geochemistry and genesis. *Ore Geol. Rev.* 106, 192–204. doi: 10.1016/j.oregeorev.2019.01.023

Wegorzewski, A. V., Grangeon, S., Webb, S. M., Heller, C., and Kuhn, T. (2020). Mineralogical transformations in polymetallic nodules and the change of Ni, Cu and Co crystal-chemistry upon burial in sediments. *Geochim. Cosmochim. Acta* 282, 19–37. doi: 10.1016/j.gca.2020.04.012

Wegorzewski, A. V., Kuhn, T., Dohrmann, R., Wirth, R., and Grangeon, S. (2015). Mineralogical characterization of individual growth structures of Mn-nodules with different Ni+Cu content from the central Pacific Ocean. *American Mineralogist.* 100, 2497–2508. doi: 10.2138/am-2015-5122

Wen, S., Chen, B., Zhang, J., Zhan, W., He, Z., and Gao, L. (2023). Systematic study on the synthesis and magnetism properties of manganese ferrite mnFe2O4 by an oxidation roasting process. *Crystals* 13, 1509. doi: 10.3390/cryst13101509

Wu, Z., Peacock, C. L., Lanson, B., Yin, H., Zheng, L., Chen, Z., et al. (2019). Transformation of Co-containing birnessite to todorokite: Effect of Co on the transformation and implications for Co mobility. *Geochim. Cosmochim. Acta* 246, 21–40. doi: 10.1016/j.gca.2018.11.001

Xiang, B., Dong, Y., Han, X., Li, X., Wang, Y., Zhang, W., et al. (2024). Enrichment of smectite in the REY–rich mud of the Clarion–Clipperton Fracture Zone in the eastern Pacific and its geological significance. *Geochem. Geophys. Geosys.* 25, e2023GC011283. doi: 10.1029/2023GC011283

Xiao, F., Simcik, M. F., and Gulliver, J. S. (2012). Perfluoroalkyl acids in urban stormwater runoff: Influence of land use. *Water Res.* 46, 6601–6608. doi: 10.1016/j.watres.2011.11.029

Xu, H., Chen, T., and Konishi, H. (2010). HRTEM investigation of trilling todorokite and nano-phase Mn-oxides in manganese dendrites. *American Mineralogist.* 95, 556–562. doi: 10.2138/am.2010.3211

Yang, Y., Liu, J., Zhu, R., Chen, Q., Wei, H., Chen, M., et al. (2023). Surface-induced oxidation of Mn(II) and crystallization of manganese (hydr)oxides on clay minerals. *Geochim. Cosmochim. Acta* 363, 129–146. doi: 10.1016/j.gca.2023.10.023

Yang, Y., Xiao, B., Shi, X., and Zhang, S. (2024). Unusual cobalt behaviors and enrichment in cobalt-rich crust from the Magellan seamounts in the Western Pacific. *Ore Geol. Rev.* 173, 106234. doi: 10.1016/j.oregeorev.2024.106234

Ye, Q., Peng, Z., Li, G., Liu, Y., Liu, M., Ye, L., et al. (2021). Rapid microwave-assisted reduction of ferromanganese spinel with biochar: Correlation between phase transformation and heating mechanism. *J. Cleaner Prod.* 286, 124919. doi: 10.1016/j.jclepro.2020.124919

Yu, L., Zhang, Y., Hudak, B. M., Wallace, D. K., Kim, D. Y., and Guiton, B. S. (2016). Simple synthetic route to manganese-containing nanowires with the spinel crystal structure. *J. Solid State Chem.* 240, 23–29. doi: 10.1016/j.jssc.2016.05.012

Zawadzki, D., Maciąg, Ł., Blasco, I., González, F. J., Wernette, B., Marino, E., et al. (2022). Geochemistry and mineralogy of ferromanganese crusts from the western cocos-nazca spreading centre, pacific. *Minerals* 12, 538. doi: 10.3390/min12050538